

# SCIENTIFIC REPORTS

OPEN

## A microfluidic device to study neuronal and motor responses to acute chemical stimuli in zebrafish

Raphaël Candelier<sup>1,2,\*</sup>, Meena Sriti Murmu<sup>3,4,5,\*</sup>, Sebastián Alejo Romano<sup>3,4,5</sup>, Adrien Jouary<sup>3,4,5</sup>, Georges Debrégeas<sup>1,2,†</sup> & Germán Sumbre<sup>3,4,5,†</sup>

Received: 17 March 2015

Accepted: 17 June 2015

Published: 21 July 2015

Zebrafish larva is a unique model for whole-brain functional imaging and to study sensory-motor integration in the vertebrate brain. To take full advantage of this system, one needs to design sensory environments that can mimic the complex spatiotemporal stimulus patterns experienced by the animal in natural conditions. We report on a novel open-ended microfluidic device that delivers pulses of chemical stimuli to agarose-restrained larvae with near-millisecond switching rate and unprecedented spatial and concentration accuracy and reproducibility. In combination with two-photon calcium imaging and recordings of tail movements, we found that stimuli of opposite hedonic values induced different circuit activity patterns. Moreover, by precisely controlling the duration of the stimulus (50–500 ms), we found that the probability of generating a gustatory-induced behavior is encoded by the number of neurons activated. This device may open new ways to dissect the neural-circuit principles underlying chemosensory perception.

One of the main goals in neuroscience is to understand how the nervous system detects, processes and converts sensory stimuli into appropriate motor patterns. To do so, it is necessary to finely control the spatiotemporal patterns of sensory stimuli while monitoring the dynamics of large neural networks in awake animal models. Among vertebrate models, zebrafish offers a unique combination of assets for such studies. The transparency and relatively small dimensions of the brain at the larval stage, and the availability of transgenic lines expressing genetically encoded calcium indicators offer the possibility to perform functional imaging at single-cell resolution of virtually the whole brain in intact behaving animals<sup>1–4</sup>.

The ability to deliver complex stimuli yet precisely controlled and with spatio-temporal structures analogous to those encountered in natural conditions is currently met only for the visual and auditory systems. In the zebrafish larva only the visual system was extensively explored where complex sensory-motor behaviors, consistent with that observed in freely swimming organisms, can be elicited by projecting natural scenes in front of an agarose-embedded larva<sup>1,5</sup>. In aquatic species chemosensation is used to find food sources<sup>6</sup>, avoid danger<sup>7</sup>, and to swallow or reject ingested particles<sup>8,9</sup>. In turbulent environments, akin to rivers, chemicals are transported in the form of fine-scale plumes such that the sequence of stimulation experienced by the fish consists of brief sporadic on/off stimuli. The time sequence of these events have been suggested to carry important information regarding the presence and location of the chemical source<sup>10</sup>.

Delivering precise sequences of sharp pulses of water-soluble chemical stimuli to a tethered larva is a non-trivial problem. Methods that rely on passive transport from a point source inevitably produce a slow and uncontrolled increase of the chemical concentration in the vicinity of the fish receptors. More

<sup>1</sup>Sorbonne Universités, UPMC Univ. Paris 06, UMR 8237, Laboratoire Jean Perrin, F-75005 Paris, France. <sup>2</sup>CNRS UMR 8237, Laboratoire Jean Perrin, F-75005 Paris, France. <sup>3</sup>Ecole Normale Supérieure, Institut de Biologie de l'ENS, IBENS, Paris, France. <sup>4</sup>INSERM, U1024, 75005 Paris, France. <sup>5</sup>CNRS, UMR 8197, 75005 Paris, France. <sup>\*</sup>These authors contributed equally to this work. <sup>†</sup>These authors jointly supervised this work. Correspondence and requests for materials should be addressed to G.S. (email: [sumbre@biologie.ens.fr](mailto:sumbre@biologie.ens.fr))

active methods expose the face of the fish to the outlet of a small tube connected to a liquid valve, allowing to sequentially deliver buffer and stimulus solutions. In this configuration, the characteristic switching time is controlled by the tube length and the flow rate. The latter being constrained by the fish dimension and the maximum flow velocity ethologically acceptable, standard macroscopic delivery systems yield switching times in the 1–10 s range (see references and discussion in Supplementary information).

Here, we designed and fabricated a microfluidic device capable of delivering multiple chemical stimuli with unprecedented spatial and temporal precision (in the 1–10 ms range) to a larva partially restrained in agarose. This stimulation microfluidic device was combined with two-photon functional imaging and high-speed video recording to simultaneously monitor the brain activity and motor behavior. We first performed a comprehensive characterization of the microfluidic device delivery dynamics and demonstrated its capability of inducing taste-specific neuronal responses in the primary gustatory center of teleost fish, the vagal lobe, without generating mechanosensory stimulation. Second, we observed that two gustatory stimuli with different hedonic values (aversive and appetitive) induced distinct activity patterns in the primary gustatory center (vagal lobe) and in higher processing areas (gustatory telencephalon, Dm). Finally, the ability to precisely control the stimulus duration allowed us to study the neuronal principles underlying gustatory-induced motor behaviors. We showed that the stimulus duration (50–500 ms) was positively correlated with the number of activated neurons in the vagal lobe, the probability of inducing a tail flip and the number of induced tail flips.

## Results

**The Microfluidic device.** The microfluidic devices (Fig. 1 and Supp. Fig. 1) were fabricated by micro-milling onto transparent acrylic (PMMA) slabs. The fluidic channels, 100  $\mu\text{m}$  in width and 25 to 200  $\mu\text{m}$  in height, were sealed by 250  $\mu\text{m}$ -thick transparent PMMA sheets using chemically-assisted thermal bonding. The circuit outlets are directed towards an open pool designed such that the larva, partially embedded in agarose, has its mouth precisely positioned in front of the delivery channel (Fig. 1d,e). The microfluidic device consists of two mostly independent circuits. The first one, driven by a push-pull syringe pump, imposes a continuous buffer flow circulating around the larva's face (blue arrows in Fig. 1e). The second circuit controls the delivery of two independent stimuli (A and B) via two electromagnetic microvalves. In the resting state, the stimulus reservoirs are at atmospheric pressure and the solutions are continuously pumped through a V-shaped channel to an underpressurized waste container. Switching a valve (injection state) overpressurizes one reservoir, triggering the instant release of the stimulus solution through the injection channel (Fig. 1b,c). Both stimuli share the same delivery outlet, thus guaranteeing that no spatial clue is associated with switching between stimuli. The device can be positioned under a two-photon microscope for simultaneous recording of neuronal activity (Fig. 1a), while a fast camera monitors the larva's tail movements from below, taking advantage of the chip's transparency.

A crucial feature of this design is the negative pressure imposed on the waste container, which drives a co-flow of the stimulus solution and the chamber fluid in the downstream arm of the V-shaped channel. Although the flow rate is relatively low (of the order of  $1 \mu\text{L}\cdot\text{s}^{-1}$ ), it prevents any cross-pollution between the buffer and the stimulus solution in the resting state, while guaranteeing through constant renewal that the stimulus solution at the entrance of the injection channels (i.e.  $\approx 600 \mu\text{m}$  from the targeted sensory receptors) remains at the desired concentration.

**Flow kinematics of the microfluidic device.** To characterize the performances of the microfluidic device we monitored the delivery of a dye-containing solution using high-speed videography. For this purpose, we switched one of the microvalves to instantly increase the pressure to  $p_{in}$  in one of the stimuli reservoirs. The time-evolution of the relative concentration, probed along a line tangential to the animal's mouth (Fig. 2a,b), exhibited a rapid transition from zero (no dye) to one (nominal dye concentration) within a few tens of milliseconds (Fig. 2c). This transition dynamics was found to be highly reproducible and showed no significant dependence on the imposed pressure  $p_{in}$  for  $p_{in} \geq 300 \text{ mbar}$ . For each value of  $p_{in}$ , we computed the onset and offset time-delays (noted  $\tau_r$  and  $\tau_d$ , respectively) defined as the delays between the valve switching and the time at which the relative concentration reached half the maximal concentration (inset of Fig. 2c). We computed the evolution of the jet width (Fig. 2d), which showed a similar dynamics towards a plateau but with a plateau value that increased quasi-linearly with  $p_{in}$ . It is worth noting that despite the jet is one order of magnitude thinner than the mouth's size, it splits in two branches close to the head surface and flows symmetrically along the exposed parts of the head. The real surface of contact is thus determined by the amount of agarose removed around the larva's mouth. Tracking the position of the dye/water interface during injection onset, we also estimated the velocity of the propagation front as a function of the distance to the mouth, for various values of  $p_{in}$  (inset of Fig. 2d).

These hydrodynamic recordings revealed several important features of the device. First, the stimulation onset and offset delays were small compared to typical gustatory stimulation times and were weakly dependent on injection overpressure. The valve switching sequence consistently drove the effective stimulus presentation sequence, albeit with a constant time delay. This device thus allows for near-millisecond precision on the stimulus presentation time, i.e. when the stimulus actually contacts the animal. The shortest stimulus duration that can be delivered by the device was  $\approx 35 \text{ ms}$ , as it corresponds to the time

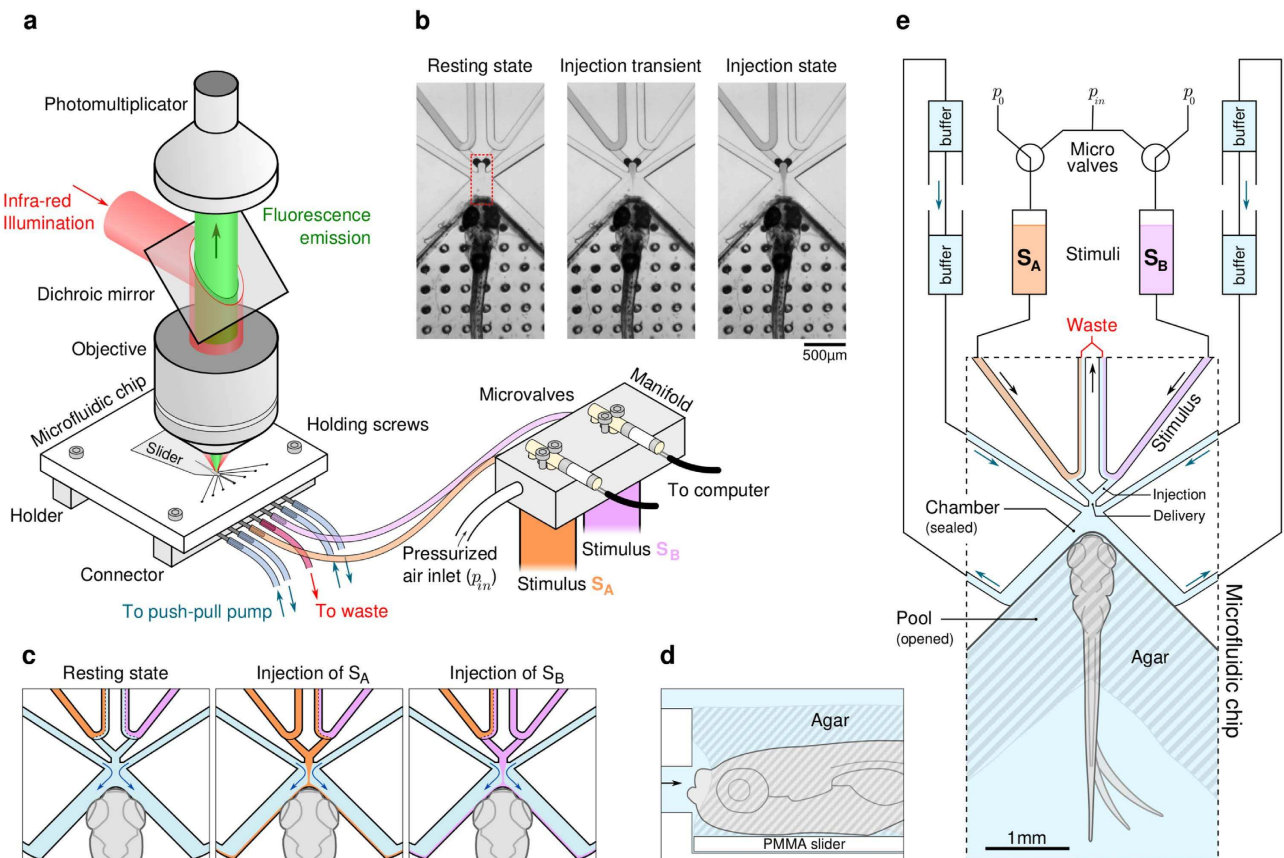


**Figure 1. Microfluidic device for precise delivery of chemical stimuli.** (a) Setup scheme: an epifluorescence two-photon microscope images neural activity while pulse-like stimuli are delivered to a zebrafish larva. An IR-sensitive camera images tail behavior from below. The microfluidic chip is connected to a computer-controlled manifold for the delivery of two different stimuli,  $S_A$  and  $S_B$ . (b) Infrared images of the device around the larva's face during injection of stimulus  $S_A$  (infrared dye, left channel).  $S_B$  (right channel) is buffer. The red rectangle indicates the region used in the kinematic view of Fig. 2a,b (c) Sketch of the fluid flow in the device during the three stationary states: at rest, during injection of  $S_A$  and during injection of  $S_B$ . (d) Side-view scheme of the larva's head resting on the movable slider. The animal's face is gently cleared before positioning. (e) Scheme of the microfluidic device: the larva's head embedded in agarose lying on the mobile slider is positioned in the pool in front of the delivery channel. Two electro-microvalves control pressures in stimulus reservoirs  $S_A$  and  $S_B$  and trigger injection.  $p_0$  is the atmospheric pressure and  $p_m > p_0$ .

needed for the injection flows to reach a stationary state. We could also generate reproducible pulses of less than 10 ms, but in this regime the maximal concentration did not reach the nominal concentration. Second, the flow velocity on the fish face was independent of the injection pressure: it was imposed by the continuous buffer flow that pinches the stimulus jet and drags it to the animal. This process guarantees that the hydromechanical stress imposed on the larva is strictly invariant during and between stimuli presentations, with no modification at pulse onset and offset, such that no artifactual mechanosensory clues should accompany the chemical stimulation.

**Gustatory neuronal responses.** To test whether the gustatory-stimulus delivery could also stimulate mechanosensory receptors, we examined gustatory-evoked neuronal responses elicited by pulse-like exposure to distinct flavours. We probed in particular the specificity of the neuronal response to gustatory inputs and the absence of associated activation of mechanosensory receptors around the larva's mouth induced by change in the flow pattern. Two-photon calcium imaging was performed on six-to-seven day old Huc:GCaMP3 transgenic larvae<sup>2</sup> first restrained in low-melting agarose (see **Sample preparation in Methods**). Prior to positioning them within the stimulation device, we carefully removed the agarose around the larva's mouth in order to expose the lips and mouth cavity, a region rich in taste buds<sup>11–13</sup>.

The two stimulation channels were first used to alternatively deliver series of five 300 ms-long pulses of sour (citric acid, 10 mM) or tasteless (buffer, control) stimuli. The most responsive primary gustatory centers in teleost fish are the facial (VII), glossopharyngeal (IX) and vagal (X) lobes<sup>14</sup>. At the developmental

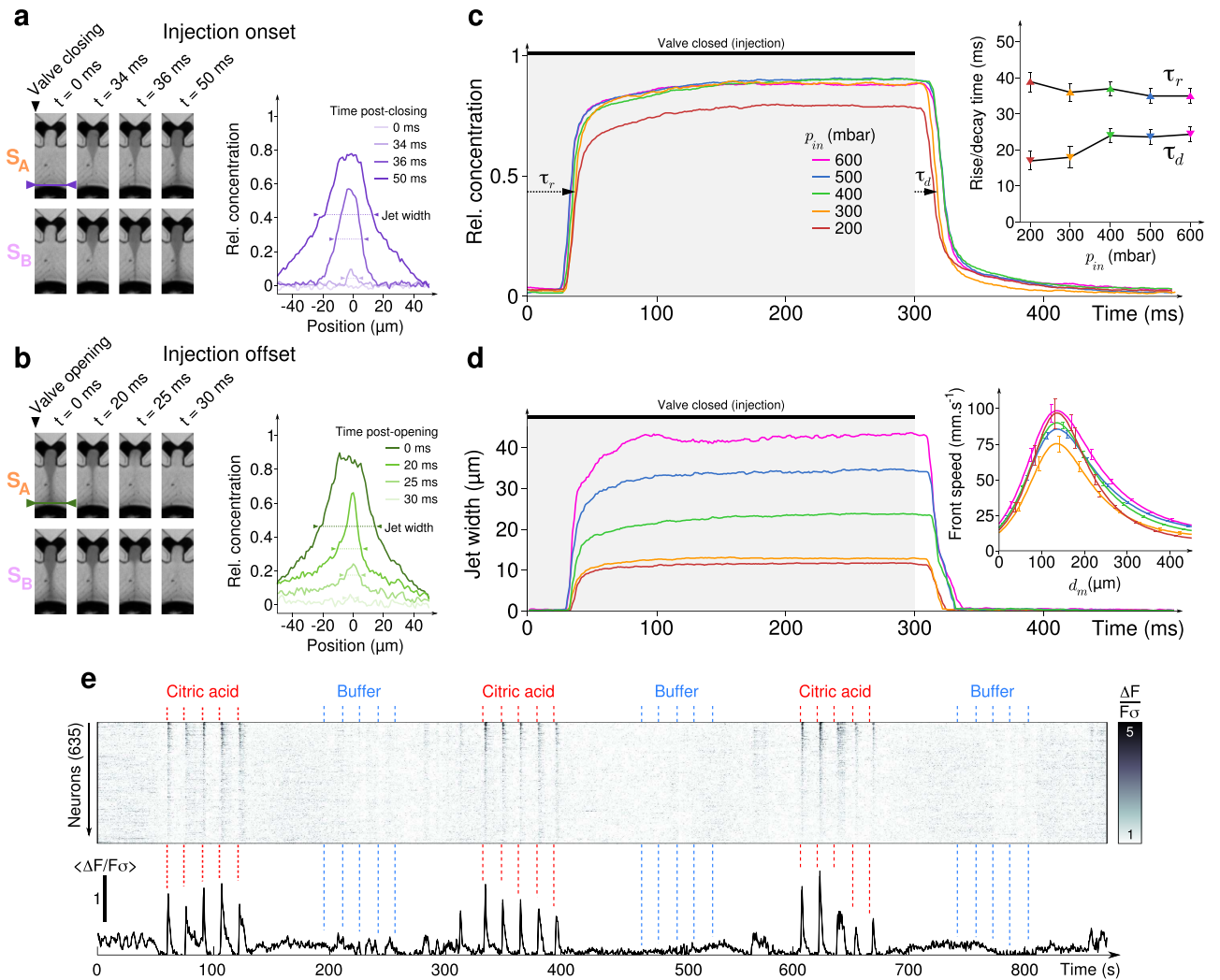


**Figure 2. Flow characterization in the microfluidic device.** (a–b) Left: kinematic view of the chamber during injection onset (a) and offset (b), for stimuli  $S_A$  and  $S_B$ , recorded with a high-speed camera. For (a–d),  $S_A$  and  $S_B$  are an IR-dye used to characterize the flow dynamics. The region of interest is highlighted on Fig. 1b: the outlet of the delivery channel is at the top while the larva's head tip is at the bottom of each frame. Right: Profiles of the relative concentration along a cross section of the chamber close to the larva's mouth (purple and green lines on the kinematic view) at different moments after closing (a) or opening (b) the micro-valves. Jet's width is defined as the width of the profile at half-maximum relative concentration. (c) Evolution of the relative concentration of the profiles shown in (a–b) for different reservoir pressures  $p_{in}$ , averaged over 5 trials. Inset: rising ( $\blacktriangle \tau_r$ ) and decay ( $\blacktriangledown \tau_d$ ) times such that the system reaches half the maximal relative concentration after microvalve switch, as a function of  $p_{in}$ . (d) Evolution of jet width for different values of  $p_{in}$ , averaged over 5 trials. Inset: Speed of the stimulus front during injection onset as a function of the distance to the larva's mouth  $d_m$ , for different  $p_{in}$ . Same color code as in (c). (e) Raster (top) and average trace (bottom) of the normalized neuronal activity  $\Delta F/F\sigma$  in the vagal lobe during alternate presentations of citric acid (CA, first stimulus  $S_A$ ) and buffer (second stimulus  $S_B$ ) at  $p_{in} = 500$  mbar. Neurons are ordered by decreasing responses to CA pulses. Similar responses were obtained for  $n = 10$  larvae. For each channel, three trains of five 300 ms-pulses separated by 15 s were delivered. Error bars: standard deviations.

stage for which the recordings were made the glossopharyngeal lobe is not yet fully-developed and is rather difficult to identify. In large-field imaging experiments (not shown) we could observe some activity in the vagal and facial lobes with acute citric acid stimulations, which suggests that most probably the stimuli activated both external (lips) and intraoral taste buds. The strongest responses were evoked in specific neuronal populations of the vagal lobe (Fig. 2e). Importantly, the control solution elicited no measurable activity, thus indicating that the measured evoked activity in the vagal lobe is solely representative of gustatory inputs rather than other variables associated with the stimulus (e.g. hydro-mechanical cues).



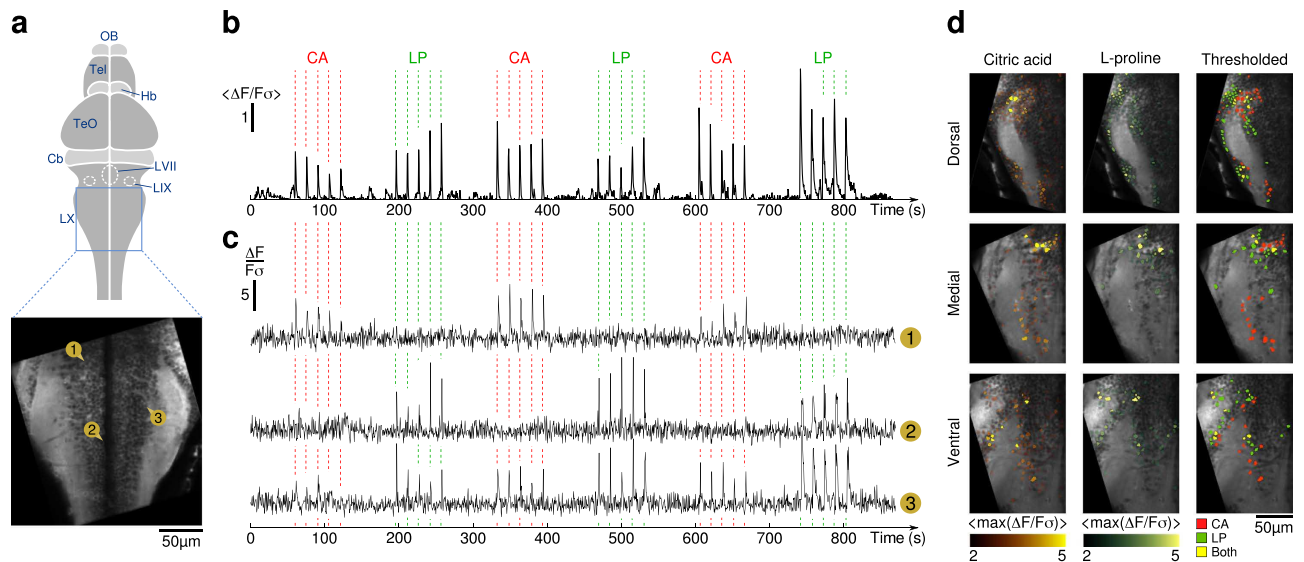


**Figure 3. Neuronal responses to chemical stimulation.** (a) Scheme of the larval brain and average fluorescence image of the vagal lobe. Neurons ① to ③, whose traces are shown in (c), are pinpointed. (b) Trace of the normalized neuronal activity averaged across all identified neurons of the vagal lobe. For each tastant, three trains of five 300 ms pulses separated by 15 s were delivered. (c) Normalized neuronal activity  $\Delta F/F\sigma$  of three neurons of the vagal lobe during alternate presentations of CA (stimulus  $S_A$ ) and LP (stimulus  $S_B$ ). Neuron ① responds exclusively to CA, ② responds exclusively to LP and ③ responds to both. (d) (Left, Middle) Maximum of  $\Delta F/F\sigma$  measured in the first 3 s following stimulus onset, averaged over 15 identical pulses, overlaid on the imaged plane (gray). (Right) Neurons responding to CA only (red), LP only (green) or both (yellow).  $p_{in} = 500$  mbar.

**Neuronal representation of gustatory stimuli with different hedonic values.** The possibility offered by the microfluidic device to rapidly alternate the presentation of two stimuli allowed us to compare between the gustatory-induced activity patterns associated with distinct gustants in a single experiment. We illustrated this capability using two stimuli of distinct hedonic values: sour aversive, citric acid (CA) and appetitive umami, L-proline (LP). We sequentially delivered series of 300 ms-long pulses of either compound while recording neuronal activity in the vagal lobe (Fig. 3). The mean signal, averaged over all identified neurons of the vagal lobe, show important responses at the population level (Fig. 3b), while at the single-cell level neuronal responses to either or both tastants have been observed (Fig. 3c). Although the topology of the gustatory-induced activity patterns appeared intermingled, we observed for three different planes (dorsal, medial and ventral) that a large fraction of neurons responded exclusively to either CA or LP, while a few responded to both (see Fig. 3d).

In the zebrafish larva, ascending projections carrying taste-related signals reach diencephalon and telencephalic areas. We thus similarly monitored CA and LP-induced responses in the dorsal telencephalic area (Supp. Fig. 3), a region known to respond to gustatory stimuli<sup>15</sup>. Interestingly, we found that even in higher gustatory centers, both CA and LP-induced responses remained relatively segregated.

**Effect of stimulus duration on gustatory-induced neuronal responses and motor behavior.** In aquatic species, the gustatory system is not only responsible for the decision of swallowing or rejecting ingested objects, but it also enables the animal to detect the location of potential food sources<sup>6</sup> or to trigger escape from dangerous chemicals and water conditions<sup>7</sup>. Large amplitude tail deflections were robustly evoked by brief exposures to CA, an aversive tastant for the larva (Supp. Movie. 3 and 4). We took advantage of the unique time-precision of the microfluidic device and its suitability for simultaneous two-photon imaging and motor behavior video-monitoring to investigate the neuronal mechanisms underlying gustatory-induced motor behaviors (Fig. 4a).

We observed that acute CA stimulation induced discrete, one-sided tail flips (see Supp. Fig. 4c, Supp. Movie. 3 and Supp. Movie. 4) sometimes followed by short series of weaker oscillations, a behavior that is reminiscent of escape responses (C-turn). These responses occurred with a probability that consistently increased with the stimulus duration (Fig. 4b). The average number of tail flips immediately following the stimulus presentation were also positively correlated with the stimulus duration (Fig. 4c). We found that the overall neuronal evoked response in the vagal lobe was larger when this was associated with a tail motor behavior. Thus, to probe the neural activity directly evoked by the gustatory inputs we separately analyzed the events that did not induce a tail flip.

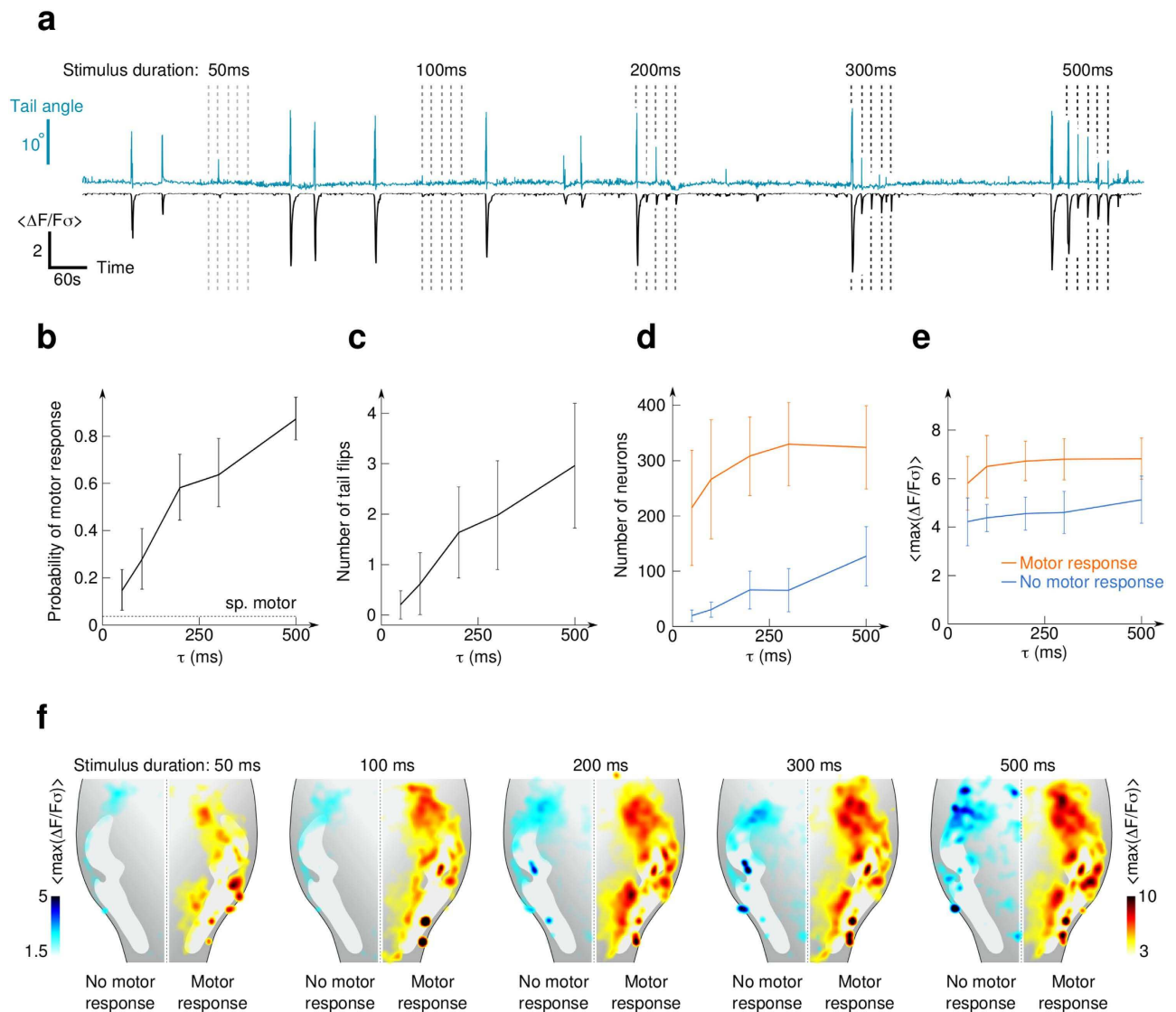


**Figure 4. Effect of stimulus duration on behavioral and neuronal responses.** (a) Time-traces of the tail angle and average normalized neuronal activity in the vagal lobe during trains of five similar stimuli of citric acid. The trains contained stimuli of increasing duration (50–500 ms). (b) Probability of observing at least one tail flip in a time interval of 3 s following the stimulus onset. The probability of a spontaneous tail movement in a random 3 s interval far from stimulation is close to zero (dashed line). (c) Average number of tail flips in a time interval of 3 s following stimulus onset. (d) Number of neurons responding to the stimulation in trials for which no motor response (blue) or a motor response (orange) was observed. (e) Amplitude of the response (defined as the maximum of  $\Delta F/F_0$  in the 3 s post-stimulation) averaged across the responsive neurons in trials associated (orange) or not associated (blue) with a motor response. (f) Topographical organization of the gustatory-evoked neuronal response patterns in the vagal lobe circuit. The color code reflects the amplitude of the response averaged across trials where no motor response was evoked (left) and trials where a motor response was observed (right) for the five different stimuli durations. For (b–f), data were pooled from 11 larvae (22 half vagal lobes) to which 25 stimuli were presented as shown in (a). The recorded area is the same as in Fig. 3. Error bars: standard deviations.  $p_m = 500$  mbar.

For trials not associated with a motor response, we observed a quasi-linear relationship between the number of activated neurons and the duration of the chemical pulses (Fig. 4d, blue). Interestingly, the  $Ca^{2+}$  transient amplitude of the responding neurons were much less affected by the stimulus duration (Fig. 4e). When the stimuli induced a tail flip, an intense and extended neuronal response was measured as shown in Fig. 4d,f. The differences in topography for gustatory-induced responses associated or not associated with motor behaviors suggest that rostral-lateral regions are associated with the sensory response while more caudo-medial ones are associated with the gustatory-induced motor response, as illustrated in Fig. 4f.

These results demonstrate that the stimulus duration is mainly encoded by the number of activated neurons in specific regions of the vagal lobe. The latter drives in a probabilistic manner a discrete transition towards a neuronal-circuit state capable of inducing a tail-flip response.

**Olfactory-induced neuronal responses in the olfactory bulb.** As a proof of concept, we performed experiments to validate the suitability of the microfluidic device for olfactory stimulation in zebrafish larvae. For this experiment, we presented to the larva's nostril two odor-specific aminoacids (lysine and phenylalanine, 300 ms pulses, 10 mM) while monitoring changes in calcium dynamics for three different focal planes of the olfactory bulb along the dorso-ventral axis (dorsal, medial and ventral). We observed that the two odorants induced distinct neuronal response patterns (Supp. Fig. 4) as previously reported<sup>16</sup>.

## Discussion

In recent years, advances in soft-microlithography techniques have led to the design of microfluidic chips for the manipulation of small organisms<sup>17</sup>. Recently, a microfluidic high-throughput system has been proposed to simultaneously immobilize and orient tens of larvae while enabling functional imaging<sup>18</sup>. The miniaturization allows for fast modifications of the flow pattern to which the specimen is exposed while still operating in the laminar flow regime and mitigate cross-diffusion between the different solutions. Microfluidic approaches were also used for chemical stimulation in *C. Elegans*<sup>19,20</sup>.

Here, we designed an open-ended microfluidic chip that combines the advantage of miniaturization for precise control over fluid flow with the possibility to perform simultaneous behavioral and neuronal activity recordings on agarose-restrained zebrafish larvae. The micro-milling method enables direct micro- and macro-patterning on a single chip, such that the microfluidic channels (in the 100  $\mu\text{m}$  range) could be directed onto an open pool (in the cm range) where the partially-restrained larva can be precisely positioned. This relatively simple fabrication method presents further advantages compared to standard soft-microlithography approaches: the circuit can sustain high pressures (in the MPa range), the channels dimensions can be adjusted in the 3 dimensions on 4 orders of magnitude with virtually no constraint on aspect ratio. These characteristics allow for precise adjustment of hydraulic resistances and flow pattern across the circuit. Furthermore, the chip can be rapidly replaced without changing the remote macro-scale delivery system (tubing, valves, pumps, stimuli reservoirs, etc.) through the use of custom-made connectors.

The capability of this chip to sequentially deliver multiple step-pulse-like stimuli, combined with whole-brain calcium imaging, opens new avenues to dissect the neuronal circuits underlying chemosensory processing in the vertebrate brain. First, it allows for the identification of tastants-specific neuronal networks across several trials and animals. This approach, which is routinely used in visual studies, was here implemented to identify neuronal circuits engaged in processing aversive versus appetitive information along the gustatory pathways.

The device unique capacity of delivering short square-pulse-like stimuli enabled us to study the neuronal mechanisms underlying gustatory-induced motor behaviors. We observed that the duration of the exposure to citric acid in the 50–500 ms range is mainly encoded by the number of recruited neurons in specific regions of the primary gustatory center, which in turn predicts both the probability of triggering an escape-like behavior and the number of induced tail movements. We thus suggest that gustatory perception in the zebrafish larva, e.g. the neuron-computational process leading to an adequate motor behaviour, takes place early in the gustatory pathway and is dictated by the number of neurons activated by the gustant.

The ability to rapidly switch between two distinct stimuli could be used in a straightforward way to study the neural processing involved in more complex stimulation sequences, and to analyse for instance how gustatory and olfactory stimuli interferes when presented with short time-lags.

Although we here focused on gustatory and olfactory neuronal processing *in vivo*, the same device can be directly used to probe the effect of transient exposure to drugs in *ex vivo* preparations. Given the large available library of zebrafish models of human syndromes, this technique has the potential to become a powerful tool for high-throughput vertebrate pharmaceutical screenings towards the development of new drugs.

## Methods

**Microfluidic chip fabrication.** The chip design has been iteratively optimized to reduce the transition times (onset and offset of delivery). The angle at which the continuous circulating buffer flow is directed in the chamber has been determined with the use of a finite-element software (Comsol). For fabrication, we used a computer-controlled micromilling machine (Minitech Mini-Mill/GX) which allows for submicronic precision, and a custom set of programs to generate G-code machine instructions. A microscope (0.75 $\times$  to 3 $\times$  Microscope Body, Edmunds Optics) and camera were mounted on the micromilling machine to allow for precise positioning ( $\approx 1\ \mu\text{m}$  in the tool axis direction) during tool change. Fabrication workflow was as follows: on a horizontal 40  $\times$  40  $\times$  4 mm PMMA slab, (i) the seven input/output through holes (600  $\mu\text{m}$ -diameter drill, KT-0236-R, PMT Microtools, USA) were drilled, (ii) an area of 25  $\times$  15 mm was surfaced with a 3 mm smoothing tool (3 mm-diameter radius-end mill, MSRS 230, NS Tools, Japan) to obtain a flat reference surface (optical grade), (iii) channels were milled

(100  $\mu\text{m}$ -diameter mill, TR-2-0040-S, PMT Microtools, USA), and finally (iv) the open chamber was milled (500  $\mu\text{m}$  and 3 mm-diameter mills, resp. TR-2-0200-S and SR-2-1181-S, PMT microtools, USA). The cover was milled out of a  $22 \times 27 \times 0.25\text{ mm}$  thin PMMA sheet (ME303005, Goodfellow) using a 500  $\mu\text{m}$ -diameter mill (TR-2-0200-S, PMT microtools, USA) to match the shape of the chamber such that the latter remains open after sealing. The chip and cover were washed three times for 5 min in 25% isopropanol and manually aligned under a microscope. Short laser pulses (45 W, Hobby 5<sup>th</sup> gen., Full Spectrum Laser, USA) were used to locally melt the PMMA at distant locations from the channels in order to secure alignment during chemically-assisted thermal bonding. Some chips used in this work were sealed with a DMSO/methanol-based melting agent, following the protocol of Ref. 21, but our most recent chips were sealed with a custom protocol that provided better resistance with a less toxic melting agent: 50% acetic acid at 65°C for 15 min under a 1.7 MPa load per chip. The chips were rinsed several times with distilled water before use.

**Flow control and measurements.** A custom brass connector (see Supp. Fig. 1-b) was screwed onto the lower side of the chip to connect the input/output channels to the pressure control manifold, the push-pull syringe pump and the waste container. The continuous buffer flow in the chamber was generated by a push-pull syringe (Legato 270, Kd Scientific), operated at a constant volumic flow rate of  $2\mu\text{L}\cdot\text{s}^{-1}$ . A custom-made duralumin manifold was used to connect the chip, the stimulus reservoirs and the microvalves. Two 3-way electro-microvalves (LHDA0533115H, The Lee Company) controlled the pressure in the stimuli reservoirs. An I/O device (Arduino UNO) was used to send TTL pulses to an amplifier connected to the microvalves and to trigger the high-speed camera. Microvalves were normally opened on atmospheric air  $p_0$  and closed on a pressure source  $p_m$ , most generally set at 500 mbar overpressure. The waste reservoir surface was positioned below the chamber, which set its pressure  $\approx -50\text{ mbar}$ . Flow recordings were performed with a high-speed camera (Fastcam APX-RS, Photron, Japan) operated at 1 kHz under infra-red light (850 nm, SFH4750, Osram). An infra-red dye (IR-806, Sigma) was dissolved in distilled water ( $c_0 = 0.34\text{ mM}$ ). Traces of precipitate were eliminated *via* filtering (0.22  $\mu\text{M}$ , Millipore). To obtain concentrations from pixel intensities, we measured the molar absorptivity of the dye solution ( $\varepsilon = 600\text{ m}^2\cdot\text{mol}^{-1}$ ) and applied Beer-Lambert's law:  $c = \log_{10}(I_0/I)/\varepsilon l$ , where  $I_0$  and  $I$  are the pixel intensities with buffer and dye and  $l$  is the thickness of the channel. Relative concentrations were computed as  $c/c_0$ . Tastant and odorant stock solutions (Sigma) were made at 100 mM in distilled water and diluted in embryo medium just before imaging to reach the concentration of 10 mM.

**Zebrafish larvae.** Transgenic zebrafish larva expressing a genetically encoded calcium indicator GCaMP3 under a pan-neuronal promoter, HuC (as described in Ref. 2) was used for all experiments. The HuC:GCaMP3GS5 line embryos were collected and raised at 28.5°C in E3 embryo medium. Larvae were kept under 14/10 hours on/off light cycles and fed after 6 d.p.f. All experiments were carried out in accordance with approved guidelines and approved by *Le Comité d'Éthique pour l'Expérimentation Animale Charles Darwin* (Ce5/2009/027).

**Retrograde Labeling.** To label the reticulospinal and vestibulospinal neurons in the hindbrain, we performed retrograde labeling by injecting a Dextran Texas Red dye (10,000 MW, Invitrogen) in the spinal cord. One day prior to imaging, 5 days-old HuC:GCaMP3 zebrafish larvae were embedded in 2% low-gelling agarose. The larva was placed on their side in a drop of Ringer solution. A 50% solution of Dextran Texas Red in 10% Ringer solution was pressure-injected *via* a glass microelectrode (10–20  $\mu\text{m}$  tip diameter) inserted into caudal spinal cord at the level of the anus using  $3 \times 100\text{ ms}$  pulses. The dye penetrated the spinal cord axons *via* the damaged axons. After injection the fish were allowed to recover and kept in fish embryo media until further use. A day later, the larva was embedded in 2% low-gelling agarose. Fluorescent-labeled reticulospinal and vestibulospinal neurons were imaged using two-photon scanning microscopy. This experiment was used as a clear landmark for the recognition of the vagal lobe  $\approx 30\text{ }\mu\text{m}$  dorso-caudally to the reticulospinal and vestibulospinal neurons (see Supp. Fig. 2).

**Sample preparation.** Six to seven days old zebrafish larvae were embedded in a drop of low-gelling agarose (2%, Sigma) on a movable slider (see Supp. Fig. 1-d). The slider was placed into an acrylic mold whose shape exactly corresponds to the pool without the channels. The larva was plunged into liquid agar at  $\approx 30^\circ\text{C}$  and a drop containing the larva was placed on the slider. The position of the larva could be slightly modified during the gelification process by moving surrounding agar with surgical tools. After some practice, we could optimize the position of the larva such that the head was very close to the slider tip and the body axis in the direction of the delivery channel. The slider was designed with an array of tiny holes (100  $\mu\text{m}$  in diameter) at the location of the specimen to provide a strong grip between the slider and agar. Once agar had gelified, we removed the slider and gently cleared the larva's face with a dissecting pin under a binocular to expose its upper and lower lips (gustatory) or nostrils (olfactory). For experiments in which behavior was recorded, the tail tip was also cleared. For imaging experiments in which we did not monitored behavior, the larva was paralyzed in 300  $\mu\text{M}$  pancuronium bromide (Tocris) added directly to the agarose. The preparation was kept in embryo medium until the slider was transferred to the microfluidic chip. A bath of embryo medium was maintained on top of the chip throughout



the experiments. During slider insertion, it was first introduced into the bath and then positioned in the pool to avoid air bubbles. All experiments were performed in the dark.

**Two-photon calcium imaging.** The two-photon microscope was based on a MOM system (Sutter) with a  $25\times$  objective (NA1.05, Olympus) and a laser tuned at  $920\text{ nm}$  (Mai Tai DeepSee Ti:Sapphire). The output power at the focal plane was less than  $3\text{ mW}$ . The filters consisted of an objective dichroic (FF705), a short-pass (IR Blocker, AFF01-680) and a band-pass filter (FF01 520/70), all from Semrock. The PMT was a H1070 (GaAsP) from Hamamatsu. The emission signal was pre-amplified with a SR-570 (Stanford Research Systems) and acquired using ScanImage at  $1.95\text{ Hz}$ , with  $256 \times 256$  pixels resolution. Recordings were made at three different optical sections,  $20\text{ }\mu\text{m}$  apart. To maintain consistency between different recordings and in different animals, each layer was identified based on several anatomical landmarks (e.g. cell density, neuropil shape and size).

**Image Processing.** Calcium imaging videos were first registered using the Turboreg plugin for ImageJ. Then, regions of interest (ROIs) corresponding to every morphologically identifiable neuron were semi-automatically defined using a custom program. In GCaMP strains, fluorescence is mainly localized in the cytosol with minimum penetration to the cellular nuclei, so we first identified individual nuclei as local intensity minima. To obtain neuronal contours we computed the Euclidean distance of each pixel to the nearest minima and performed a watershed segmentation. ROIs typically included neuronal nuclei and a thin cytosolic surrounding ring, excluding the outermost cytosolic perimeter that could potentially be subject of cross-neuron fluorescence contamination due to high neuronal density. The obtained ROIs were manually inspected and corrected when necessary. Eventually, the fluorescence traces were computed as the average intensity over each ROI. To record motor behavior, a miniature microscope connected to a fast infrared camera ( $120\text{ Hz}$ , TXG02, Baumer) was placed below the micro-fluidic device. We computed the raw orientation of the binarized image of the tail, and tail angle was defined as the deviation from the baseline orientation<sup>22,23</sup>. The tail beats after each pulse were counted by eye. All algorithms were written in Matlab.

**Neuronal data analysis.** A baseline fluorescence signal was estimated for each neuron by computing the  $8^{\text{th}}$  percentile of fluorescence traces  $F(t)$  in sliding windows of  $15\text{ s}$ <sup>24</sup>. The resulting smooth curve  $b(t)$  locally approximated the baseline level and reflected slow fluctuations unrelated to the fast calcium transients evoked by neuronal activity. The relative variation of fluorescence intensity was calculated as  $\Delta F/F = (F - b)/b$ . In a typical experiment, trains of stimulations separated by  $15\text{ s}$  alternate with phases without stimulation. We defined the resting times as the set of times for which no stimulation was delivered in the previous  $15\text{ s}$ . For each neuron, we computed the standard deviation of the relative variation of fluorescence during resting times  $\sigma = \text{std}(\Delta F/F)_{\text{rest}}$  and the normalized relative variation of fluorescence intensity  $\Delta F/F\sigma$ . To isolate neurons responding to a stimulation pulse, we computed  $m$  the maximum of  $\Delta F/F\sigma$  in the first 3 seconds post-stimulation (seven images). To determine which neurons were significantly responding, we performed a Kolmogorov-Smirnov test to determine whether each value of  $m$  could arise from the distribution of the maximum of a set of seven normally distributed random points. A maximum of  $m = 3.189$  corresponds to a p-value of 0.01, and was chosen as the responding threshold. For each fish, both sides of the time-averaged image of the vagal lobe were semi-manually registered onto a virtual “average” half-vagal lobe. Average patterns of activity were then obtained by convoluting the discrete field  $\sum_i m_i \delta(x_i, y_i)$  of neurons stemming from several animals (11 larvae, hence 22 half-vagal lobes) with a Gaussian kernel of width  $\sigma_k = 4.2\text{ }\mu\text{m}$  and unit height. These maps were normalized by the density map, computed as the convolution of  $\sum_i \delta(x_i, y_i)$  with a Gaussian kernel of width  $2\sigma_k$  and height  $1/\sigma_k^2$ .

## References

- Ahrens, M. B. *et al.* Brain-wide neuronal dynamics during motor adaptation in zebrafish. *Nature* **485**, 471–477 (2012). doi: 10.1038/nature11057.
- Panier, T. *et al.* Fast functional imaging of multiple brain regions in intact zebrafish larvae using Selective Plane Illumination Microscopy. *Frontiers in Neural Circuits* **7** (2013). doi: 10.3389/fncir.2013.00065.
- Ahrens, M. B., Orger, M. B., Robson, D. N., Li, J. M. & Keller, P. J. Whole-brain functional imaging at cellular resolution using light-sheet microscopy. *Nat Methods* **10**, 413–420 (2013).
- Portugues, R., Feierstein, C. E., Engert, F. & Orger, M. B. Whole-Brain Activity Maps Reveal Stereotyped, Distributed Networks for Visuomotor Behavior. *Neuron* **81**, 1328–1343 (2015). doi: 10.1016/j.neuron.2014.01.019.
- Bianco, I. H., Kampff, A. R. & Engert, F. Prey capture behavior evoked by simple visual stimuli in larval zebrafish. *Front Syst Neurosci* **5**, 101 (2011).
- Paris, C. B. *et al.* Reef Odor: A Wake Up Call for Navigation in Reef Fish Larvae. *PLoS ONE* **8**, e72808 (2013).
- Egan, R. J. *et al.* Understanding behavioral and physiological phenotypes of stress and anxiety in zebrafish. *Behavioural Brain Research* **205**, 38–44 (2009).
- Finger, T. E. Feeding patterns and brain evolution in ostariophysian fishes. *Acta Physiol Scand Suppl* **638**, 59–66 (1997).
- Finger, T. E. Sorting food from stones: the vagal taste system in Goldfish, *Carassius auratus*. *J. Comp. Physiol. A Neuroethol. Sens. Neural. Behav. Physiol.* **194**, 135–143 (2008).
- Vergassola, M., Villermaux, E. & Shraiman, B. I. ‘Infotaxis’ as a strategy for searching without gradients. *Nature* **445**, 406–409 (2007).
- Ishimaru, Y. *et al.* Two families of candidate taste receptors in fishes. *Mechanisms of Development* **122**, 1310–1321 (2005).

12. Aihara, Y. *et al.* Transgenic labeling of taste receptor cells in model fish under the control of the 5'-upstream region of medaka phospholipase C-beta 2 gene. *Gene Expression Patterns* **7**, 149–157 (2007).
13. Hansen, A., Reutter, K. & Zeiske, E. Taste bud development in the zebrafish, *Danio rerio*. *Developmental Dynamics* **223**, 483–496 (2002).
14. Evans, D. H., Claiborne, J. B. & Currie, S. *The Physiology of Fishes*. CRC Marine Biology Series (CRC Press, 2013), fourth edition edn.
15. Wullimann, M. F. & Mueller, T. Teleostean and mammalian forebrains contrasted: Evidence from genes to behavior. *The Journal of Comparative Neurology* **475**, 143–162 (2004).
16. Blumhagen, F. *et al.* Neuronal filtering of multiplexed odour representations. *Nature* **479**, 493–498 (2011). doi: 10.1038/nature10633.
17. Rohde, C. B., Zeng, F., Gonzalez-Rubio, R., Angel, M. & Yanik, M. F. Microfluidic system for on-chip high-throughput whole-animal sorting and screening at subcellular resolution. *Proceedings of the National Academy of Sciences* **104**, 13891–13895 (2007).
18. Lin, X. *et al.* High-throughput mapping of brain-wide activity in awake and drug-responsive vertebrates. *Lab Chip* **15**, 680–689 (2015). doi: 10.1038/nature11057.
19. Chronis, N., Zimmer, M. & Bargmann, C. Microfluidics for *in vivo* imaging of neuronal and behavioral activity in *Caenorhabditis elegans*. *Nature methods* **4**, 727–731 (2007).
20. Albrecht, D. R. & Bargmann, C. I. High-content behavioral analysis of *Caenorhabditis elegans* in precise spatiotemporal chemical environments. *Nat Meth* **8**, 599–605 (2011). doi: 10.1038/nmeth.1630.
21. Brown, L., Koerner, T., Horton, J. H. & Oleschuk, R. D. Fabrication and characterization of poly(methylmethacrylate) microfluidic devices bonded using surface modifications and solvents. *Lab Chip* **6**, 66–73 (2006).
22. McElligott, M. & O'Malley, D. Prey Tracking by Larval Zebrafish: Axial Kinematics and Visual Control. *Brain, Behavior and Evolution* **66**, 177–196 (2005).
23. Burgess, H. A. & Granato, M. Modulation of locomotor activity in larval zebrafish during light adaptation. *Journal of Experimental Biology* **210**, 2526–2539 (2007).
24. Dombeck, D. A., Khabbaz, A. N., Collman, F., Adelman, T. L. & Tank, D. W. Imaging large-scale neural activity with cellular resolution in awake, mobile mice. *Neuron* **56**, 43–57 (2007).

## Acknowledgements

We thank HC Park (Kyungpook National University, Korea) for the HuC promoter, L. Looger (Howard Hughes Medical Institute, Ashburn, Virginia, USA) for GCaMP3 and K. Kawakami (National Institute of Genetics, Shizuoka, Japan) for pT2KXIGin vector. We thank N. Garroum for helpful assistance in simulating the flows in the microfluidic device during chip design, V. Perez-Schuster for help with the data analysis of two-photon calcium imaging, T. Pietri for helpful discussions, and M. Kapsimali for assistance in neuroanatomy of the zebrafish gustatory system. The post-doc work of M.S.M. was supported by *Neuropôle de recherche francilien* (NeRF) and INSERM. One year of post-doc work of R.C. was supported by the *Fondation Pierre-Gilles de Gennes pour la recherche*. G.S. was funded by the ERC starting grant 243106. ANR-10-LABX-54 MEMO LIFE, ANR-11-IDEX-0001-02 PSL\* Research University.

## Author Contributions

R.C. designed the microfluidic chip, characterized the flows, analyzed the neuronal and behavioral data and contributed to manuscript writing. M.S.M. performed functional imaging and behavioral experiments, analyzed neuronal and behavioral data and contributed to manuscript writing. S.A.R. wrote the neuron detection and signal extraction programs. A.J. wrote the tail tracking program. G.D. and G.S. designed the project and contributed to manuscript writing.

## Additional Information

**Supplementary information** accompanies this paper at <http://www.nature.com/srep>

**Competing financial interests:** The authors declare no competing financial interests.

**How to cite this article:** Candelier, R. *et al.* A microfluidic device to study neuronal and motor responses to acute chemical stimuli in zebrafish. *Sci. Rep.* **5**, 12196; doi: 10.1038/srep12196 (2015).



This work is licensed under a Creative Commons Attribution 4.0 International License. The images or other third party material in this article are included in the article's Creative Commons license, unless indicated otherwise in the credit line; if the material is not included under the Creative Commons license, users will need to obtain permission from the license holder to reproduce the material. To view a copy of this license, visit <http://creativecommons.org/licenses/by/4.0/>

# A microfluidic device to study neuronal and motor responses to acute chemical stimuli in zebrafish.

Raphaël Candelier<sup>1,2,†</sup>, Meena Sriti Murmu<sup>3,4,5,†</sup>, Sebastián Alejo Romano<sup>3,4,5</sup>, Adrien Jouary<sup>3,4,5</sup>, Georges Debrégeas<sup>1,2,‡</sup> and Germán Sumbre<sup>3,4,5,‡</sup>

<sup>1</sup>Sorbonne Universités, UPMC Univ. Paris 06, UMR 8237, Laboratoire Jean Perrin, F-75005 Paris, France

<sup>2</sup>CNRS UMR 8237, Laboratoire Jean Perrin, F-75005 Paris, France

<sup>3</sup>Ecole Normale Supérieure, Institut de Biologie de l'ENS, IBENS, Paris, France

<sup>4</sup>INSERM, U1024, 75005 Paris, France

<sup>5</sup>CNRS, UMR 8197, 75005 Paris, France

May 28, 2015

## Movie captions

### Movie 1

Delivery of a single pulse of a dye-containing solution, recorded at  $1\text{ kHz}$ . The valve (not visible) opens for  $100\text{ ms}$  and the solution contacts the fish face for  $85\text{ ms}$ .

### Movie 2

Delivery of multiple  $50\text{ ms}$ -long pulses of two dye-containing solutions, recorded at  $500\text{ Hz}$ . The two microvalves are activated alternatively to trigger sequential injections from both channels. Channel 1 opens for  $50\text{ ms}$  at  $t = 100, 500$  and  $900\text{ ms}$ , channel 2 opens for  $50\text{ ms}$  at  $t = 300, 700$  and  $1100\text{ ms}$ . Solutions contact the fish face for  $\approx 25\text{ ms}$ .

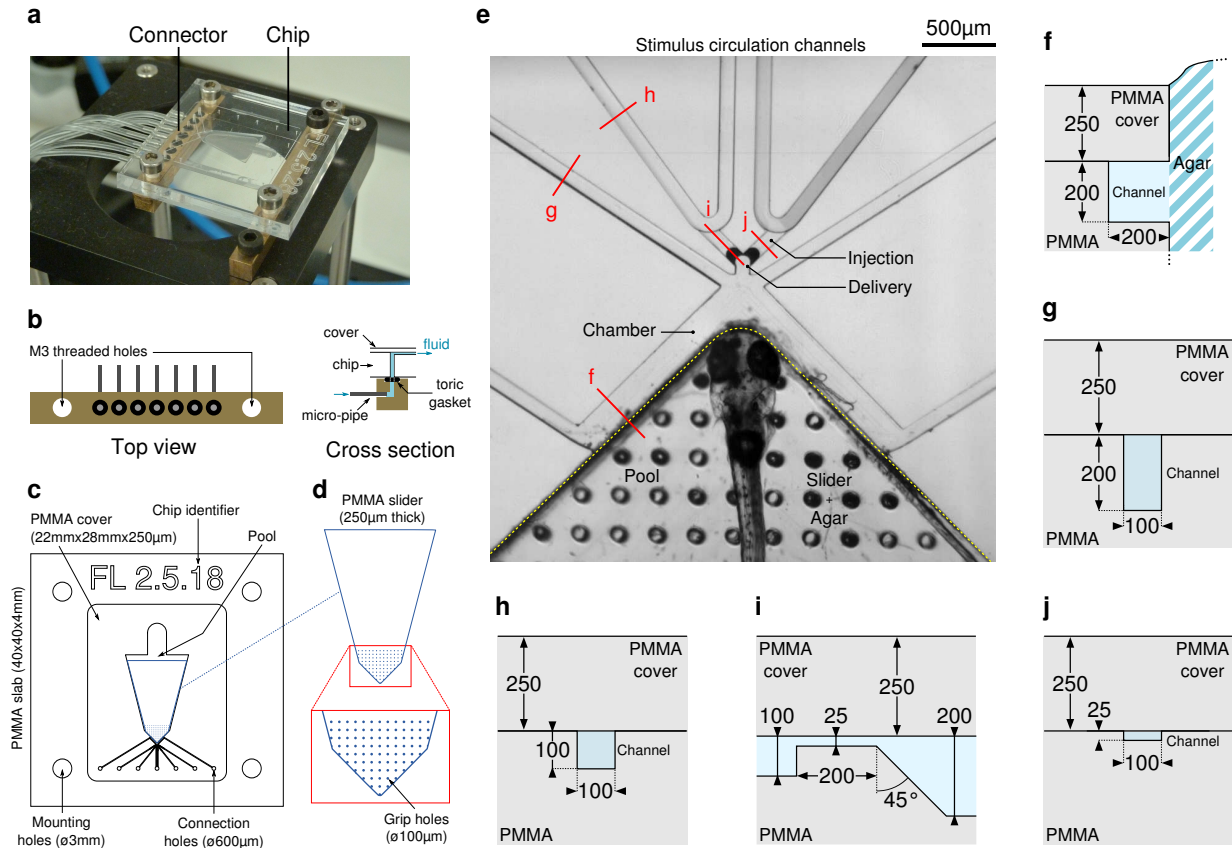
### Movie 3

Behavioral response to  $300\text{ ms}$ -long pulses of citric acid, recorded at  $50\text{ Hz}$ . The tail of the larva is freed from agar, and its absolute angular trace is displayed in blue on the bottom-right plot. Five stimuli, indicated by the red rectangles, are delivered at  $t = 5, 10, 15, 20$  and  $25\text{ s}$ . Robust behavioral responses appear approximatively  $500\text{ ms}$  after each stimulus onset. Spontaneous bursts of behavioral activity sporadically occur.

### Movie 4

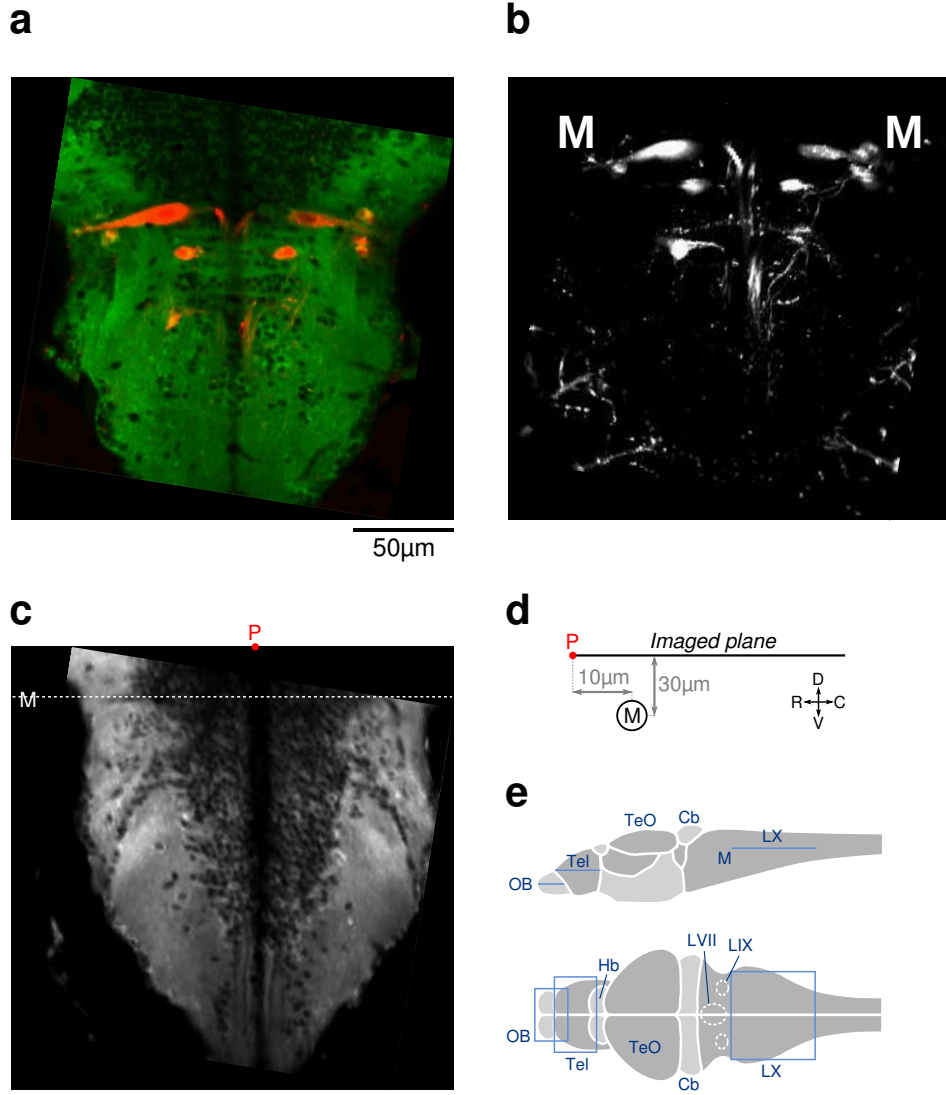
Simultaneous recordings of neuronal and behavioral responses to  $300\text{ ms}$ -long pulses of citric acid. The traces of the normalized neuronal activity  $\Delta F/F\sigma$  averaged over all neurons (yellow) and the tail angle (magenta) are displayed on the bottom plot. Five pulses-like stimuli, indicated by grey rectangles, are delivered at  $t = 18, 33, 48, 63$  and  $78\text{ s}$ .

## Supplementary Figures

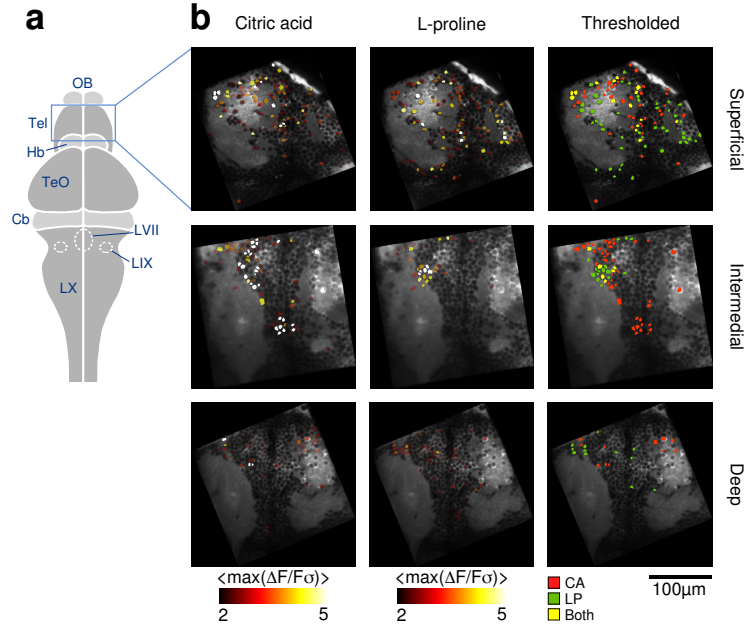


**Supplementary Figure 1.** Detailed description of the microfluidic chip. **(a)** Picture of the chip mounted on the brass connector (left) and the brass holder (right). **(b)** Top view and cross section schemes of the connector. The brass part is  $40 \times 5 \times 5 \text{ mm}$  and micro-pipes have an external diameter of  $600 \mu\text{m}$ . Toric gaskets prevent leakage when the chip is screwed onto the connector. **(c)** Scheme of the chip. It is made of a micro-milled PMMA slab sealed with a thin PMMA cover. **(d)** Scheme of the larva-holding slider. The blow-up shows the grip holes at the slider tip, which ensure a strong binding of the agar drop. **(e)** Microfluidic channels around the larva's head. The dashed yellow line indicates the separation between the sealed part (covered) and the pool (not-covered), in which the slider holding the agaros-embedded larva is inserted. Red segments indicate locations of the cross-sections displayed in panels (f-j). **(f-j)** Cross section schemes of the different channels. In (f) one wall of the chamber channel is made of gelified agarose. It is replaced by the larva's face at the slider tip. The  $45^\circ$  slope in (i), visible as a dark spot in (e), prevents the formation of vortices and stagnant volumes in the delivery channel.

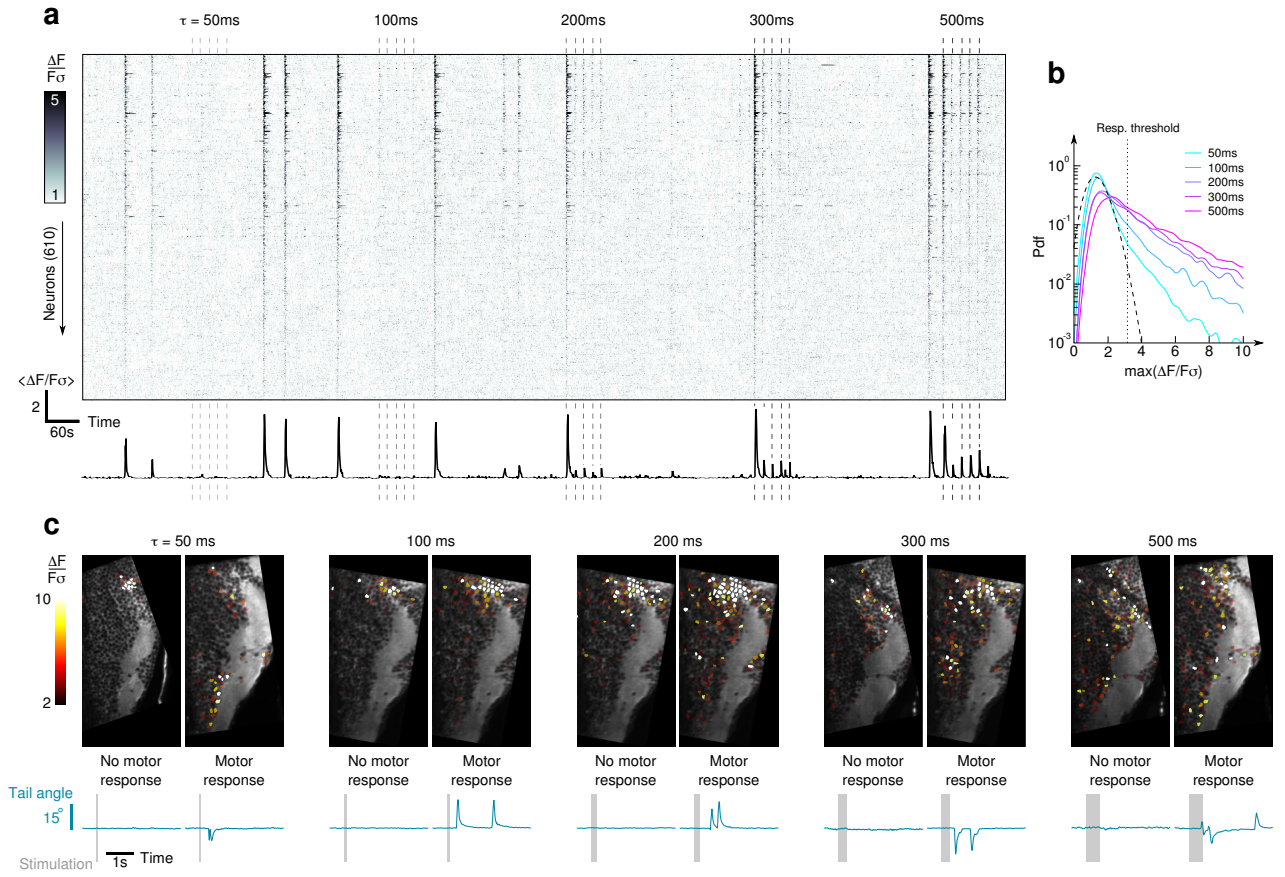




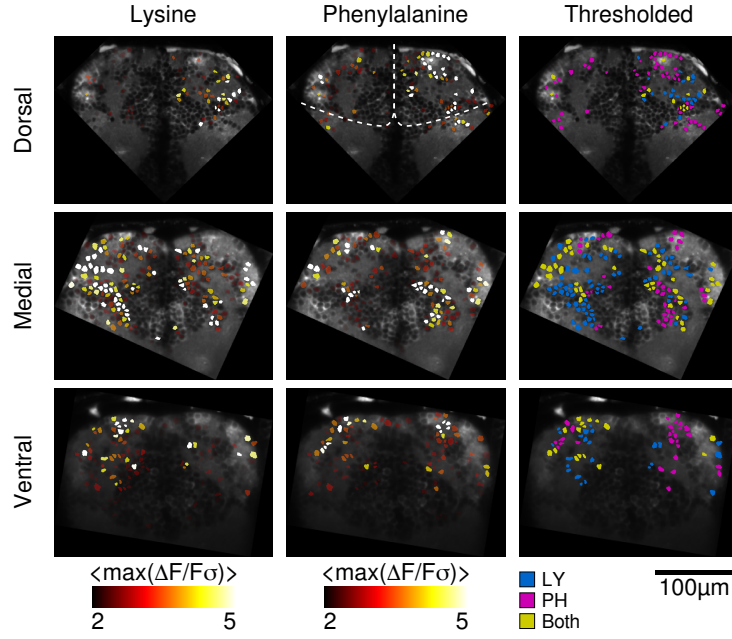
**Supplementary Figure 2.** Localization of the recorded brain regions. (a, b) Fluorescence images of reticulospinal neurons retrogradely labeled with Dextran Texas-red. Mauthner cells (M) are clearly recognized. (c) Image of the vagal lobe obtained by two-photon microscopy. Recordings were made in areas that lied  $\approx 30 \mu m$  dorsally with respect to the reticulospinal and the vestibulospinal neurons, whose approximative dorso-ventral location is represented with a dashed line. (d) Scheme of the position of the imaged plane with respect to Mauthner cells (sagittal view). The virtual point *P* is also represented in panel c for correspondence. (e) Schemes of the larva's brain and areas where neuronal recordings were performed (blue rectangles). OB = olfactory bulb, Tel = telencephalic lobes, Hb = habenula, TeO = optic tectum, Cb = cerebellum, LVII = facial lobe, LIX = glossopharyngeal lobe, LX = vagal lobe, M = Mauthner cell.



**Supplementary Figure 3.** Gustatory responses in the superficial, intermedial and deep layers of the dorsal telencephalon evoked by 300 ms-pulses of citric acid (CA) and L-proline (LP). The three focal planes were imaged 20μm apart, thus a total depth of 40μm. (a) Scheme of the larva brain. The recorded region is highlighted by a blue rectangle. (b) *Left, Middle* Maximal value of  $\Delta F/F\sigma$  measured in the first 3 s post-stimulation, averaged over  $n = 15$  presentations, overlaid on the time-average fluorescence signal (grey image). *Right* Neurons responding to either CA only (red), LP only (green) or both (yellow).  $p_{in} = 500 \text{ mbar}$ .

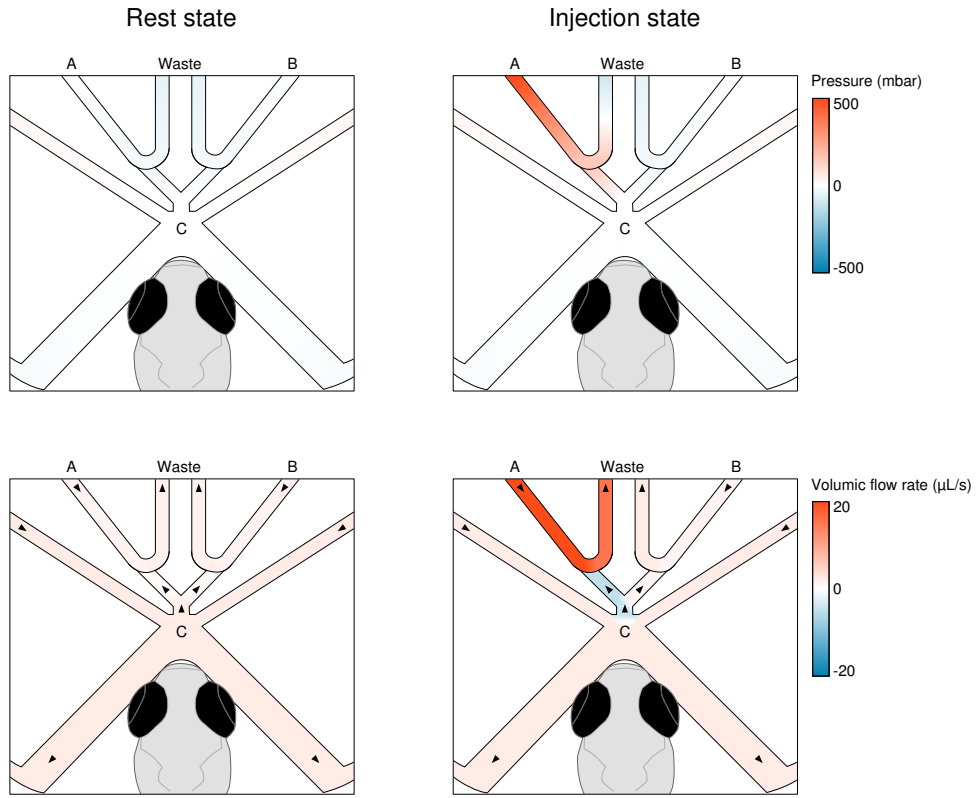


**Supplementary Figure 4.** Additional information on the effect of stimulus duration. **(a)** Raster plot (top) and  $\Delta F/F\sigma$  averaged across neurons (bottom) for the same experiment as in **Fig. 4-a**. **(b)** Distributions of the maximal values of  $\Delta F/F\sigma$  in the 3 s post-stimulation for the different stimuli durations. The black dashed curve is the distribution of maximum values of normally distributed random noise. The dotted vertical line indicates the responding threshold (3.189). **(c)** Examples of neuronal and behavioral responses to citric acid stimuli.

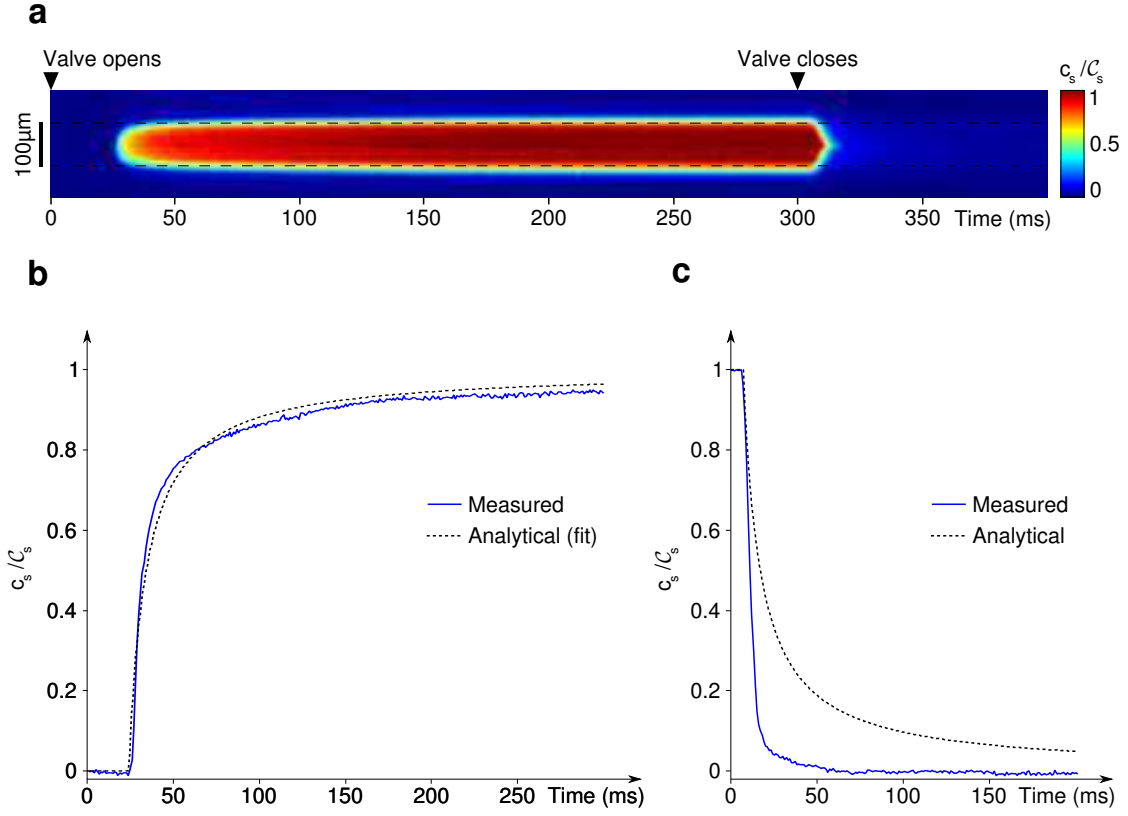


**Supplementary Figure 5.** Olfactory responses in the dorsal, medial and ventral regions of the olfactory bulb evoked by 300 *ms*-pulses of Lysine (LY) and Phenylalanine (PH). **(Left, Middle)** Maximal value of  $\Delta F/F\sigma$  measured in the first 3 *s* post-stimulation, averaged over  $n = 15$  presentations, overlaid on the time-average fluorescence signal (gray image). The dashed white line indicate the boundary between the olfactory bulb and the telencephalic lobes. **(Bottom)** Neurons responding to either LY only (blue), PH only (purple) or both (yellow).  $p_{in} = 500$  *mbar*.





**Supplementary Figure 6.** Pressure (top) and flow rates (bottom) fields for the two stationary states, at rest (left) and during injection (right), determined with eq. 1 and eq. 4. The boundary conditions are  $p_B = 0 \text{ mbar}$ ,  $p_D = -0.05 \text{ mbar}$ ,  $p_w = -50 \text{ mbar}$  and  $p_A = 0 \text{ mbar}$  in the resting state. In the injection state,  $p_A$  is set to  $500 \text{ mbar}$ . In the bottom panel, small black arrows indicate the direction of positive flow rate in each channel, defined as the direction of flow rate in the resting state.



**Supplementary Figure 7.** (a) Evolution of the relative concentration profile close to the outlet of the delivery channel as a function of time, measured in the chamber of our microfluidic device. The position of the 100  $\mu\text{m}$  channel outlet is shown with black-dashed horizontal lines. (b) Evolution of the average relative concentration profile of stimulus  $c_s/C_s$  at the onset of stimulus delivery, close to the outlet of the delivery channel. The analytical curve is a fit corresponding to eq. 9b with  $\tau = 10.2 \text{ ms}$ . (c) Evolution of the average relative concentration profile of stimulus  $c_s/C_s$  at the offset of stimulus delivery, close to the outlet of the delivery channel. The analytical curve corresponds to eq. 9a with the same  $\tau$  as in (b).

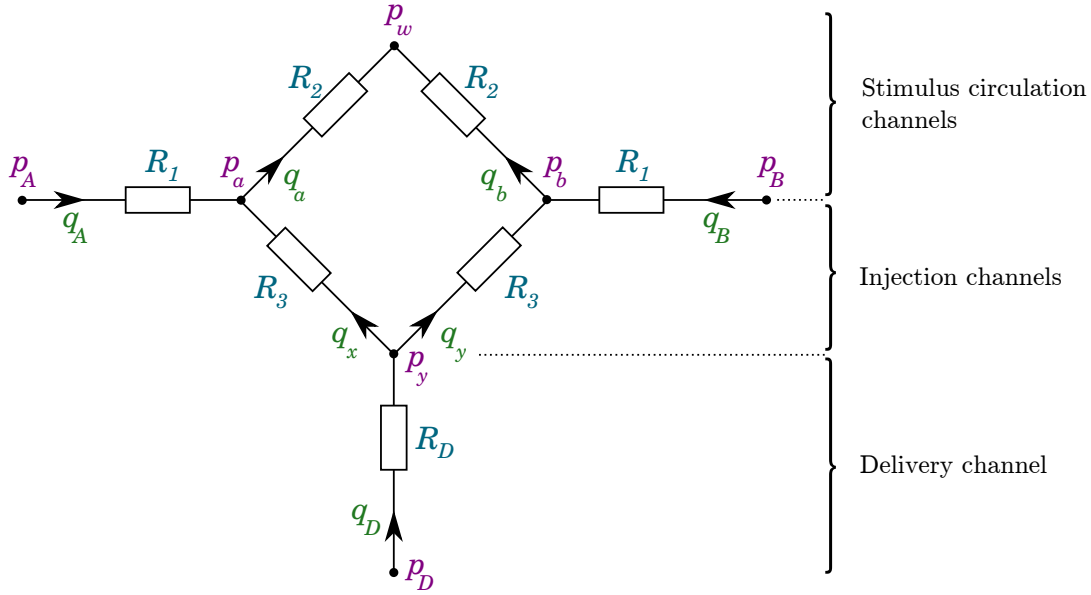
# Supplementary information

## Fluid dynamics of chemical delivering

### Stationary flows

Our microfluidic system has two stationary states, namely resting and injection, depending on the pressure applied to the solution reservoirs. In this section, we derive analytical expressions for pressure and volumic flow rates in all channels for both states, which provides a complete description of the flows inside the chip.

The hydrodynamics in the chamber channels and the delivery circuit are rather decoupled, such that these circuits can be separated. The microfluidic delivery circuit can be synthesized by the following diagram, where  $P$ ,  $q$  and  $R$  stand for pressure (all expressed as offsets to the atmospheric pressure), volumic flow rate and hydraulic resistance:



**Supplementary diagram 1.** Equivalent diagram of the delivery circuit. Pressures are defined at the nodes and each channel is described by its hydraulic resistance  $R$  and flow rate  $q$ . Arrows indicate the direction of positive flow rates, defined as the direction of fluid in the resting state.

The pressures of the stimuli reservoirs  $p_A$  and  $p_B$  and of the waste  $p_w$  are directly controlled by the operator, while the pressure at the end of the delivery channel  $p_D$  is very close to atmospheric pressure<sup>1</sup>. The pressures  $p_a$ ,  $p_b$  and  $p_y$  are set internally. For each of the seven segments the Hagen–Poiseuille relation applies :

$$\Delta p = Rq \quad (1)$$

where the hydraulic resistance  $R$  of a rectangle channel of width  $w$ , height  $h$  and length  $L$  is defined by :

$$R = \frac{8\mu L}{\pi} \left( \frac{w+h}{wh} \right)^4 \quad (2)$$

with  $\mu = 10^{-3} \text{ Pa.s}$  the dynamic viscosity of water. In units of  $10^8 \text{ mbar.s.m}^{-3}$ , the hydraulic resistances are  $R_1 = 170$ ,  $R_2 = 132$ ,  $R_3 = 320$  and  $R_D = 1.3$ .

We obtain three more equations with flow conservation:

$$q_A + q_x = q_a \quad (3a)$$

$$q_B + q_y = q_b \quad (3b)$$

$$q_D = q_x + q_y \quad (3c)$$

<sup>1</sup> $p_D$  is controlled by the flow rate in the chamber such that  $p_D = -\rho_w q_{ch}^2 / 2S_{ch}^2$ , with  $\rho_w$  the volumic mass of water,  $q_{ch} = 2\mu L.s^{-1}$  the flow rate in the chamber and  $S_{ch} = 4.10^{-8} \text{ m}^2$  the surface of the cross-section of the chamber channel, which gives  $p_D = -0.05 \text{ mbar}$ .

The system of ten linear equations in eq.1 and eq.3 can be solved. Introducing the reduced quantities  $\alpha = \frac{R_3}{R_D}$ ,  $\gamma_1 = \frac{R_2 R_3}{R_1 R_2 + R_2 R_3 + R_1 R_3}$ ,  $\gamma_2 = \frac{R_1 R_3}{R_1 R_2 + R_2 R_3 + R_1 R_3}$  and  $\gamma_3 = \frac{R_1 R_2}{R_1 R_2 + R_2 R_3 + R_1 R_3}$ , the internal pressures write:

$$p_y = \frac{\alpha p_D + \gamma_1(p_A + p_B) + 2\gamma_2 p_w}{\alpha + 2(\gamma_1 + \gamma_2)} \quad (4a)$$

$$p_a = \gamma_1 p_A + \gamma_2 p_w + \gamma_3 p_y \quad (4b)$$

$$p_b = \gamma_1 p_B + \gamma_2 p_w + \gamma_3 p_y \quad (4c)$$

The pressures and flow rates in the chamber circuit can be calculated in a similar way. All pressures and flow rates are displayed on **Supplementary Figure 6**, in both the resting and injection states.

The flow rate at the outlet of the delivery channel  $q_D$  follows an affine dependence with the pressure applied in the stimulus reservoir :  $q_D = a.p_A + b$ , with  $a = -1.10 \times 10^{-11} \text{ m}^3.\text{mbar}^{-1}.\text{s}^{-1}$  and  $b = 1.42 \times 10^{-9} \text{ m}^3.\text{s}^{-1}$ . At the typical pressure at which recordings have been performed ( $p_A = 500 \text{ mbar}$ ) we found  $q_D = -4.08 \mu\text{L}.\text{s}^{-1}$ . Conversely, the reservoir pressure at which the outlet flow becomes negative, *i.e.* the minimal pressure for which the system is injecting stimulus in the chamber, is at  $p_A^{\text{min}} = 128 \text{ mbar}$ . This is coherent with the minimal pressure found experimentally, namely  $125 \text{ mbar}$ .

## Comparison with standard injection methods

In this section, we discuss how the dynamical aspects of our system compares with methods that have been most commonly used for delivering chemicals to aquatic species.

### Methods with uncontrolled advection/diffusion

A class of methods is based on local concentration increase, either *via* a solid media (*e.g.* soaked cotton pellets [1, 2], freeze-dried pellets [3], starch gel[4], agar gel [5]) or by directly releasing drops of the product in the sample tank [6].

The transport of chemical compounds involves two distinct mechanisms, advection and diffusion [7]. In most cases, advection is a much faster transporting process, and diffusion can be neglected. In the previously cited methods, advection processes are not controlled (flows created in the fluid during product release, movements of the animal, thermal convection, etc.) which introduce a huge variability in the front propagation speed and important concentration heterogeneity. These methods are viable in studies where temporal aspects or control of the concentration are not important, but a precise understanding of the gustatory neuronal processes requires a better level of control. Hence, to generate sharp and reproducible chemical stimulations, it is crucial to control the advection processes around the specimen.

In addition, in advection-based delivery systems where the chemical is stored very close to the sample, care should be taken to eliminate diffusion-based cross-pollution. Indeed, diffusion should be avoided for two reasons: (i) since the propagation front spreads with time, the concentration at a given point slowly increases which makes it difficult to define an onset time of stimulation, and (ii) since diffusion is an irreversible process, without proper cleaning of the chemoreceptors the delivery cannot be repeated on the same animal, which hampers multi-trials averaging. Diffusion is a rather slow process<sup>2</sup>, but can appear during the course of a experiment. In our microfluidic device, the distance between the stimuli circulation channels and the larva's mouth is  $\approx 375 \mu\text{m}$ , so a front of stimulus could reach the sample in a few minutes. Our system has thus been designed such that in the resting state a permanent flow is maintained in the injection and delivery channels to suck water from the chamber ( $q_x$ ,  $q_y$  and  $q_D$  are positive), which completely eliminates diffusion-based cross-pollution, while the flow around the sample is unchanged between the resting and injection states.

### Valve-driven injection

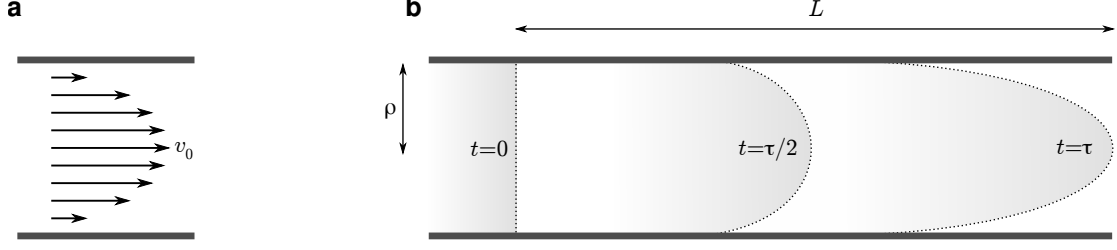
Common advection-based methods involve a switching valve system (see *e.g.* [9, 10] for the gustatory system or [11, 12, 13] for the olfactory system). In these devices a continuous flow is set into an injection tube, and the fluid (buffer or stimulus) is switched at the inlet of the injection tube. The valve prevents cross-diffusion between the buffer and the stimulus solution and ensures a constant flow rate around the specimen. In this section, we compute the evolution of the concentration at the outlet of such an injection tube and show that it has a slow evolution, which we compares to measurements in our device.

Let us consider a cylindrical tube of length  $L$  and internal radius  $\rho$  in which a continuous flow is imposed at a constant flow rate  $q$  (see **Supplementary diagram 2**). We also assume that at time  $t = 0$ , solution  $A$

<sup>2</sup>For instance, citric acid has a diffusion coefficient of  $D \simeq 0.65 \times 10^{-9} \text{ m}^2.\text{s}^{-1}$  in water[8], which gives a propagation of the diffusion front in  $\approx 15 \text{ s}$  for a distance of  $100 \mu\text{m}$ , and  $\approx 385 \text{ s}$  for a distance of  $500 \mu\text{m}$ .

<sup>3</sup>Similar results are found with rectangular channels, though the calculus is more complicated. See [14] for details.





**Supplementary diagram 2.** (a) Velocity profile of a Poiseuille, laminar flow. (b) Scheme of the evolution of a planar front in an injection tube.

is switched to solution  $B$  using a perfect valve at the entrance of the tube, forming a planar front. The front deforms as solution  $B$  progresses in the tube with a Poiseuille flow profile :

$$v(r) = v_0 \left( 1 - \left( \frac{r}{\rho} \right)^2 \right) \quad (5)$$

where  $v_0$  is the maximum velocity, at the center of the tube. With this expression the flow rate can be derived as a function of  $v_0$  :

$$q = \int_0^\rho 2\pi r v(r) dr = 2\pi \rho^2 v_0 \int_0^1 (1-x) dx = \frac{\pi \rho^2 v_0}{2} \quad (6)$$

At  $t = \tau$ , the front tip reaches the outlet of the injection tube. This time is defined by :

$$\tau = \frac{L}{v_0} = \frac{\pi L \rho^2}{2q} \quad (7)$$

Let us note  $\mathcal{C}_A$  and  $\mathcal{C}_B$  the concentrations of solutions  $A$  and  $B$ . We aim at computing the time-evolution of the average concentrations  $c_A(t)$  and  $c_B(t)$  at the tube outlet :

- For  $t < \tau$ , we have :  $c_A(t) = \mathcal{C}_A$  and  $c_B(t) = 0$ .
- For  $t \geq \tau$ , the concentrations are given by :

$$c_A(t) = \mathcal{C}_A \left( 1 - \left( \frac{r_f(t)}{\rho} \right)^2 \right) \quad (8a)$$

$$c_B(t) = \mathcal{C}_B \left( \frac{r_f(t)}{\rho} \right)^2 \quad (8b)$$

where  $r_f(t)$  is the radius of the cross section of the front at the outlet of the tube. The radius  $r_f(t)$  corresponds to a velocity of exactly  $v(r_f(t)) = L/t$ , which gives, by using the expression of the Poiseuille profile in eq. 5 :

$$\frac{L}{t} = v_0 \left( 1 - \left( \frac{r_f}{\rho} \right)^2 \right)$$

hence :

$$\begin{aligned} \frac{L}{t} &= v_0 \frac{c_A(t)}{\mathcal{C}_A} \\ \frac{L}{t} &= v_0 \left( 1 - \frac{c_B(t)}{\mathcal{C}_B} \right) \end{aligned}$$

and, finally :

$$c_A(t) = \mathcal{C}_A \frac{L}{v_0 t} = \mathcal{C}_A \frac{\tau}{t} \quad (9a)$$

$$c_B(t) = \mathcal{C}_B \left( 1 - \frac{L}{v_0 t} \right) = \mathcal{C}_B \left( 1 - \frac{\tau}{t} \right) \quad (9b)$$

The evolution of the concentrations at the outlet in  $t^{-1}$  imposes a slow-exchange dynamics, and the system continues to deliver a significant concentration of the initial compound  $A$  for a long time after offset. Given the sensitivity of gustatory chemoreceptors<sup>4</sup>, this implies that sensory activation can still occur even at a very long time after the valve switch have replaced the stimulus with the buffer. For instance, with a tube of length  $10\text{ cm}$ , inner radius  $1\text{ mm}$  and a flow rate of  $10\text{ }\mu\text{L.s}^{-1}$ , we get  $\tau = 15.7\text{ s}$  and after  $315\text{ s}$  the liquid presented to the specimen would still contain 5% of the original solution. To significantly decrease the characteristic time  $\tau$ , it is necessary to reduce the size of the injection channel. Reducing the channel radius  $\rho$  has a strong limitation, since at a given flowrate the bulk velocity  $v_0$  will increase quadratically and rapidly exceed the limit of physiologically relevant values ( $\approx 50\text{ mm.s}^{-1}$ ). So if  $\rho$  decreases,  $q$  has to be decreased accordingly, such that there is no net effect on the timescale  $\tau$ . The only acceptable strategy is therefore to reduce the length of the delivery channel  $L$ . By using microfluidic devices, typical values of  $L$  decrease from  $\approx 10\text{ cm}$  to  $\approx 100\text{ }\mu\text{m}$ , yielding three orders of magnitude in  $\tau$ . As shown in **Supplementary Figure 7-b**, in our system the onset of stimulus presentation follows the slow evolution of eq. 9 with a typical time  $\tau \approx 10\text{ ms}$ .

Finally, one important asset of our microfluidic device is that it completely eliminates the stimulus in a few tens of milliseconds at injection offset, as shown in **Supplementary Figure 7-b**. This is due to the inversion of flow direction in the injection and delivery channels, which stops any arrival of the stimulus in the chamber and eliminates the stagnant volume at the outlet of the delivery channel, combined with the continuous washing of the specimen with clean buffer.

Altogether, our system allows for the delivery of pseudo-square pulses at an almost constant concentration with unprecedented steep-rising and falling edges and it allows for a complete cleaning of the specimen in a few tens of milliseconds after stimulus presentation. The high-level of control over advection offered by microfluidic systems is used here to (i) deliver several pulses of stimuli in a very reproducible fashion to the same animal, which greatly facilitates response-averaging across trials, and (ii) deliver pulses as short as  $10\text{ ms}$ , which is impossible with standard techniques. Finally, as the delivery channel has an extremely short length ( $100\text{ }\mu\text{m}$ ) it is cleaned very fast and be used for the delivery of another chemical in a very short delay following the first stimulus.

---

<sup>4</sup>Approximately  $0.5\text{ }\mu\text{M}$  for amino-acids chemoreceptors [15].

## References

- [1] Jones, K. A. The palatability of amino acids and related compounds to rainbow trout, *Salmo gairdneri* Richardson. *Journal of Fish Biology* **34**, 149–160 (1989).
- [2] Jones, K. A. Chemical requirements of feeding in rainbow trout, *Oncorhynchus mykiss* (Walbaum); palatability studies on amino acids, amides, amines, alcohols, aldehydes, saccharides, and other compounds. *Journal of Fish Biology* **37**, 413–423 (1990).
- [3] Mackie, A. & Mitchell, A. Further studies on the chemical control of feeding behaviour in the Dover Sole, *Solea solea*. *Comparative Biochemistry and Physiology Part A: Physiology* **73**, 89–93 (1982).
- [4] Hidaka, I., Ohsugi, T. & Kubomatsu, T. Taste receptor stimulation and feeding behaviour in the puffer, *Fugu pardalis* I. Effect of single chemicals. *Chemical Senses* **3**, 341–354 (1978).
- [5] Mearns, K. J., Ellingsen, O. F., Døving, K. B. & Helmer, S. Feeding behaviour in adult rainbow trout and Atlantic salmon parr, elicited by chemical fractions and mixtures of compounds identified in shrimp extract. *Aquaculture* **64**, 47–63 (1987).
- [6] Braubach, O. R., Wood, H.-D., Gadbois, S., Fine, A. & Croll, R. P. Olfactory conditioning in the zebrafish (*Danio rerio*). *Behavioural Brain Research* **198**, 190–198 (2009).
- [7] Bennett, T. D. *Transport by Advection and Diffusion* (Wiley, 2012).
- [8] Haynes, W. *CRC Handbook of Chemistry and Physics, 93rd Edition*. CRC Handbook of Chemistry and Physics (Taylor & Francis, 2012).
- [9] Chervova, L. S. & Lapshin, D. N. The Threshold Sensitivity of External Chemoreceptor in Carp *Cyprinus carpio* to Amino Acids and Classical Gustatory Substances. *Journal of Ichthyology* **45**, S307–S314 (2005).
- [10] Oike, H. *et al.* Characterization of Ligands for Fish Taste Receptors. *The Journal of Neuroscience* **27**, 5584–5592 (2007).
- [11] Li, J. *et al.* Early Development of Functional Spatial Maps in the Zebrafish Olfactory Bulb. *The Journal of Neuroscience* **25**, 5784–5795 (2005).
- [12] Mack-Bucher, J. A., Li, J. & Friedrich, R. W. Early functional development of interneurons in the zebrafish olfactory bulb. *European Journal of Neuroscience* **25**, 460–470 (2007).
- [13] Yaksi Emre, Francisca, v. S. P., Niessing Jorn, Bundschuh Sebastian T & Friedrich Rainer W. Transformation of odor representations in target areas of the olfactory bulb. *Nat Neurosci* **12**, 474–482 (2009). 10.1038/nn.2288.
- [14] FM, W. *Viscous fluid flow*, 123 (McGraw-Hill Book Company, 1974).
- [15] Caprio, J. *et al.* The taste system a the channel catfish: from biophysics to behavior. *TINS* **16**, 192–197 (1993).